https://doi.org/10.5194/ar-2026-1
Preprint. Discussion started: 26 January 2026

AEROSOL Research Discussions

Numerical study of the collection of aerosol particles by falling deformable drops

Thibaut Ménard[1], Emmanuel Reyes[1], Wojciech Aniszewski[1], Pascal Lemaitre[2], and Emmanuel Belut[3]

[1]University of Rouen-Normandie, CORIA - UMR 6614 CNRS, St-Étienne-du-Rouvray, 76800, France
[2]Autorité de Sûreté Nucléaire et de Radioprotection (ASNR), PSN-RES/SCA/LPMA, F-91400, Saclay, France
[3]Institut National de Recherche et de Sécurité (INRS), Vandoeuvre-lès-Nancy, 54500, France

Correspondence: Emmanuel Belut (emmanuel.belut@inrs.fr)

Abstract. The free fall of a drop through gas loaded with solid particles gives rise to multiple physical interactions, which remain poorly documented, esp. when the drop is no longer spherical. In particular, no model predicts the particle collection efficiency for drops undergoing deformations or oscillations. This study aims to contribute to this effort by investigating numerically the dynamics of water drops freely falling in air laden with dispersed solid particles, for drop Reynolds and Weber number such that drops present deformations/oscillations or not (e.g., $Re = 30$, 70, 500 and 876). An Eulerian-Lagrangian framework is adopted. The drop internal and external flows are simulated with Direct Numerical Simulation (DNS), and the dynamics of the liquid/gas interface are tracked using a combination of the Volume of Fluid (VOF) and Level Set methods, this approach predicts the interface dynamics in line with experimental data. The trajectories of solid particles are simulated using Lagrangian tracking and taking into account drag, gravity, and Brownian motion. For spherical drops with Reynolds numbers below 200, our methodology replicates previous results. In the presence of oscillations/deformations, the flow parameters of the two continuous phases are correctly predicted. The particle collection efficiency also follows the experimental trend, but the values differ significantly from measurements found in the literature. We therefore propose certain areas of improvement with the goal of obtaining better fits to the available experimental data.

1 Introduction

In many industrial and environmental contexts, the air is loaded with aerosol pollutants, such as dust, smoke, pathogens, or radioactive particles. Workers thus frequently face exposure to air polluted with aerosol particles, which can cause serious health risks, leading to respiratory problems and other adverse health effects. During nuclear accidents, a significant amount of radioactive materials can also be released into the environment in the form of aerosol particles that can ultimately be inhaled by humans, with harmful health effects. Reducing particulate emissions and concentration in the air is a central issue for which effective control methods are needed. In these contexts, the washout or scrubbing of aerosol particles by free-falling drops is a standard process to decrease the concentration of airborne aerosol particles (Greenfield (1957)).

At the scale of a single drop, the effectiveness of this process, and the primary purpose of this study, is modeled with a micro-physical parameter called *collection efficiency*, E. It is defined as the ratio between the number of aerosol particles collected by a falling drop and the total number of particles in the volume swept up by the drop. In the literature, Slinn (1977)

https://doi.org/10.5194/ar-2026-1
Preprint. Discussion started: 26 January 2026

AEROSOL Research Discussions

was the first to establish models to calculate this efficiency, using particle flow balances, assuming potential flows around the drop and a decoupling of the collection mechanisms. The limitations of this approach were partially overcome in later work. Grover and Pruppacher (1977) were the first to theoretically establish collection efficiencies based on Lagrangian tracking of particles around drops by calculating DNS flows for spherical drops, with Reynolds numbers below 200, taking into account drag and electric forces on aerosols. However, they did not consider Brownian motion in their Lagrangian tracking despite its influence on sub-micron particles. More recently Minier and Peirano (2001) integrated analytically the approach of Langevin (1908) for Brownian motion of aerosols. Thanks to this approach, Cherrier et al. (2016) added Brownian motion to the Grover and Pruppacher (1977) approach, and their results were validated with efficiency measurements performed in the laboratory by Dépée et al. (2021).

Despite this conceptual unification, a major scientific challenge remains. These approaches require an accurate simulation of the flow around the drop. However, drops with a Reynolds number above 500 oscillate at high frequencies and deform progressively (Szakáll et al., 2010). For such a task, the methods deployed by Cherrier et al. (2016) and Dépée et al. (2021) – relying on a fixed geometry – are no longer valid. Our work proposes an alternative method to extend computations to include Reynolds numbers above 200. The liquid/gas interface dynamics are now modeled using a hybrid Volume of Fluid (VOF) - Level Set methods (CLSVOF, here in a momentum-conserving variant published by Vaudor et al. (2017)), coupled to a DNS solver applied to both continuous phases. In contrast, the motion of the discrete aerosol phase is modeled in the same Lagrangian framework as introduced by Cherrier et al. (2016), accounting for the drag force and Brownian motion.

To validate this approach, tests are first carried out to ensure that the model predictions stay within the state of the art. First, free-falling water drops of Reynolds 30 and 70 exhibiting no oscillation nor deformation are simulated as they interact with aerosol particles with aerodynamic diameters ranging from 2 nm to 20 μm. The drop settling velocities and velocity fields inside and outside the drop are compared with results from the literature (Beard, 1976; Cherrier et al., 2016). Similarly, the aerosol collection efficiencies are compared with results from the literature (Cherrier et al., 2016). Tests of the independence of the results concerning the numerical resolution parameters are carried out (mesh convergence and interpolation order). Secondly, simulations are performed for flow regimes with drop oscillation and deformation (drop Reynolds of 500 and 876), for which – to our knowledge – no simulation results of aerosol particle collection efficiency are available in the literature. For these regimes, the simulation results for the continuous phases are validated by comparison with experimental results as done by Ren et al. (2020) (terminal fall velocity, mean drop axis-ratio, and characteristic oscillation frequencies (Beard, 1976; Szakáll et al., 2010)) . For the aerosol phase, the collection efficiencies are compared with experimental results from the literature (Quérel et al., 2014; Lai et al., 1978), considering the poly-dispersion of the aerosol sizes involved.

This approach to evaluate the proposed method is described in the Results section of the manuscript, after a presentation of the physical modeling of the system under consideration and the numerical methods used for its approximate resolution.

2 Physical model

Our simulations consider a free-falling drop in quiescent air at atmospheric pressure ($P = P_{atm} = 101\,kPa, T = 293,15\,K$).

https://doi.org/10.5194/ar-2026-1
Preprint. Discussion started: 26 January 2026

AEROSOL Research Discussions

2.1 Continuous phase

The motion of the continuous phases, consisting of both, inner flow (water) and outer flow (air), is simulated by solving numerically the same Navier-Stokes equations, assuming incompressibility :

$$\begin{cases} \dfrac{\partial \rho(\psi)\boldsymbol{U}}{\partial t} + \boldsymbol{\nabla}\cdot(\rho(\psi)\boldsymbol{U}\otimes\boldsymbol{U}) = -\boldsymbol{\nabla}p + \boldsymbol{\nabla}\cdot(2\mu(\psi)D) + \rho(\psi)\boldsymbol{g} + \sigma\kappa(\psi)\delta(\psi)\boldsymbol{n} \\ \boldsymbol{\nabla}\cdot\boldsymbol{U} = 0 \end{cases} \tag{1}$$

where ρ, $\boldsymbol{U}$ and p are the density, velocity and pressure, respectively, $D = \frac{1}{2}(\boldsymbol{\nabla U} + \boldsymbol{\nabla U}^T)$ is the strain rate tensor, μ the dynamic viscosity, $\rho(\psi)\boldsymbol{g}$ the gravity forces. The surface tension forces are considered expressed by $\sigma\kappa(\psi)\delta(\psi)\boldsymbol{n}$, with σ the surface tension, $\kappa(\psi)$ the local curvature of the interface and $\delta(\psi)$ the Dirac function. ψ is the phase indicator which is used to reconstruct the interface at each time step, it can be either the Level Set function (ϕ) or the VOF function (C) depending the quantity (ρ, μ, ...) to be determined (Vaudor et al., 2017).

On present simulations, the absolute velocity of both fluids are calculated in the drop reference frame. The convective velocity in the equations must, therefore, be $\boldsymbol{U} - \boldsymbol{U}_d$ where $\boldsymbol{U}_d$ is the instantaneous velocity of the drop calculated at each time step. The equations are hence transformed as follows:

$$\frac{\partial \rho(\psi)\boldsymbol{U}}{\partial t} + \boldsymbol{\nabla}\cdot(\rho(\psi)(\boldsymbol{U}-\boldsymbol{U}_d)\otimes\boldsymbol{U}) = -\boldsymbol{\nabla}p + \boldsymbol{\nabla}\cdot(2\mu(\psi)D) + \rho(\psi)\boldsymbol{g} + \sigma\kappa(\psi)\delta(\psi)\boldsymbol{n} \tag{2}$$

The numerical resolution of equation 1 requires determining a function ψ. An additional equation (4) is solved concurrently to achieve this. This equation specifically deals with the transport and evolution of the interface by the flow between the different phases (in our case, the boundary between air and water) within the computational domain. The parameter ψ can represent either the interface distance function Level Set (ϕ) or VOF (C) functions, which are coupled as described by Sussman and Puckett (2000). The interface is defined by zero level set surface/curve ($\phi = 0$ in 3D/2D respectively)), and the VOF function represents the volume fraction of liquid in a cell:

$$C = \frac{1}{V}\int_V H(\phi)dV \tag{3}$$

where H is the Heaviside function equal to 1 in the liquid and 0 in the air. Advection of both functions is achieved by solving the following equation :

$$\frac{\partial \psi}{\partial t} + \nabla\cdot(\boldsymbol{U}-\boldsymbol{U}_d)\psi = 0 \tag{4}$$

which is coupled with and additional equation to preserve the distance function property of the Level Set ($||\nabla\Phi|| = 1$) (Sussman et al. (1994); Min and Gibou (2007)). Physical parameters are computed with the help of the VOF function, while geometrical characteristics with either the Level Set function or the VOF function:

https://doi.org/10.5194/ar-2026-1
Preprint. Discussion started: 26 January 2026

AEROSOL Research Discussions

$$\rho(C) = C\rho_l + (1-C)\rho_g$$

$$\mu(C) = C\mu_l + (1-C)\mu_g$$

$$\boldsymbol{n} = \frac{\nabla\phi}{|\nabla\phi|}$$

$$\kappa(\phi) = \nabla.\boldsymbol{n}$$

$$\delta(\psi)\boldsymbol{n} = \nabla C$$

2.2 The Discrete Phase

A Lagrangian approach is used to model the transport of aerosol particles by the continuous phases. Each aerosol particle is treated as a discrete entity, and its motion is governed by drag forces and Brownian motion. The state vector of each particle is $\boldsymbol{Z}_p(t) = \{\boldsymbol{x}_p(t), \boldsymbol{U}_p(t)\}$, where $\boldsymbol{x}_p(t)$ is the instantaneous position of the particle in the flow and $\boldsymbol{U}_p(t)$ its velocity. Smaller particles (sizes below $1\mu m$) are sensitive to Brownian effects, while larger ones follow their inertia. The equations of motion retained correspond to the Langevin equations:

$$\begin{cases} d\boldsymbol{x}_p = (\boldsymbol{U}_p(t) - \boldsymbol{U}_d(t))\, dt \\ d\boldsymbol{U}_p = \dfrac{\boldsymbol{U}_f(t) - \boldsymbol{U}_p(t)}{\tau_p} dt + B d\boldsymbol{W}(t) \end{cases} \tag{5}$$

where $\boldsymbol{U}_f$ is the fluid velocity at the particle's position, τ_p is the relaxation time of the particle (taking into account Cunningham correction for rarefaction effect). The last term of the equation represents the Brownian effects, with $d\boldsymbol{W}$ the increment of the Wiener process and B the diffusion coefficient Minier and Peirano (2001). Effectively, this represents a one-way coupled system which is justified at the volume fraction considered in our work as shown in Elgobashi (1984).

2.3 Capture criteria

In our modeling framework, the particles are considered "collected" as long as they enter into geometrical contact with the drop, which is in line with theoretical predictions (Wang et al., 2015). In order to determine if the particles enter into contact with the drop during the Lagrangian tracking, the Level-Set value at the particle location (ϕ_p) is compared at each time step. Hence, the capture condition can be expressed as:

$$\phi_p + r_p \geq 0, \tag{6}$$

which – considering that ϕ is (by choice) set as negative outside of the droplet – means simply that its surface contacts the particle (which is closer to it than its radius r_p). Once that happens, the trajectory calculation for the particle is terminated, and the particle is considered captured by the falling drop. This formulation accounts for the varying shape and size of the drop throughout its deformation process.

https://doi.org/10.5194/ar-2026-1
Preprint. Discussion started: 26 January 2026

AEROSOL Research Discussions

2.4 Collection efficiency

For each particle diameter, the collection efficiency E is defined as the ratio between the particle number flow rate collected by the drop during its fall and the particle number flow rate in the cross-section of the drop. During a single Lagrangian particle release, N_{inj} particles are injected in the upstream flow of the drop. These particles are injected homogeneously inside a
110 "virtual disk" placed generally upstream of the drop (as detailed in section 4.3), afterwards, E is computed from:

$$E(d_d, d_p) = \frac{N_{capt}(d_p)}{N_{inj}(d_p)}, \tag{7}$$

where N_{capt} is the number of particles captured by the drop, while d_d and d_p are the drop and particle diameter respectively.

https://doi.org/10.5194/ar-2026-1
Preprint. Discussion started: 26 January 2026

AEROSOL Research Discussions

3 Numerical Methods

3.1 Continuous phases

The simulations in this study are conducted using an in-home academic code ARCHER (Academic Research Code for Hydrodynamic Equations Resolution), originally created by a team led by Alain Berlemont (Tanguy and Berlemont, 2005; Ménard et al., 2007; Vaudor et al., 2017). It is aimed to carry out DNS (Direct Numerical Simulation) simulations for multiphase flow simulations with a range of interface representations ((Aniszewski et al., 2014)) and multitude of physical phenomena (Duret et al. (2013)). Many implementation details can be found in Vaudor et al. (2017). In Archer, the temporal integration is carried out using either Euler or 2nd order Runge-Kutta scheme. Volume of Fluid (VOF) and Level Set interface tracking functions are first advected explicitly to allow the calculation of physical parameters at time $n+1$. Then a projection method is used by introducing an intermediate velocity $\boldsymbol{U}^*$ to solve the momentum equation without the pressure term (Eq. 8), and the velocity $\boldsymbol{U}^{n+1}$ and pressure correction (Eq. 9).

$$\boldsymbol{U}^* = \frac{\rho^n \boldsymbol{U}^n}{\rho^{n+1}} + \frac{\Delta t}{\rho^{n+1}} \left(\boldsymbol{\nabla} \cdot (\rho(C)\boldsymbol{U} \otimes \boldsymbol{U}) + \boldsymbol{\nabla} \cdot (2\mu(C)D)\right)^n + \frac{\Delta t}{\rho^{n+1}} \Big((\rho(C) - \rho_g)\boldsymbol{g} + \sigma\kappa(\phi = 0)\delta(\psi)\boldsymbol{n} \Big)^{n+1} \tag{8}$$

$$\boldsymbol{U}^{n+1} = \boldsymbol{U}^* - \Delta t \left(\frac{\boldsymbol{\nabla} p^{n+1}}{\rho^{n+1}} \right) \tag{9}$$

The discretization of the convective term, the WENO scheme, is employed based on the conservative discretization described by Vaudor et al. (2017). The Standard CSF method Popinet (2018) is used to handle the surface tension term, where $\delta(\psi)\boldsymbol{n}$ is approximated by $\boldsymbol{\nabla} C$ (see also (**?**)).

Applying the divergence operator to Eq. 9, and with the help of continuity equation $\boldsymbol{\nabla}.\boldsymbol{U}^{n+1} = 0$, allows to write the following Poisson equation (10) which yields the pressure field. The velocity field $\boldsymbol{U}^{n+1}$ is deduced with Eq. 9.

$$\boldsymbol{\nabla}. \left(\frac{\boldsymbol{\nabla} p^{n+1}}{\rho^{n+1}} \right) = \frac{\boldsymbol{\nabla} \cdot \boldsymbol{U}^*}{\Delta t} \tag{10}$$

The velocity field and the interface distance values (given by the Level-Set ϕ) are discretized on a uniform Cartesian mesh ($\Delta x = \Delta y = \Delta z$). In our program, the Marker and Cell (Welch et al., 1965) method is used: scalar quantities (VOF, distance function, pressure) are located at mesh centers, while vector quantities are positioned on the faces, resulting in a a staggered mesh (Figure 1).

3.2 Discrete phase

A discretized version of (5), proposed by Mohaupt et al. (2011), is used to track the trajectories of the particles. The discretized version involves numerical approximation methods to solve the equations and calculate the particle positions and velocities at each time step:

https://doi.org/10.5194/ar-2026-1
Preprint. Discussion started: 26 January 2026

$$\begin{cases} \boldsymbol{x}_p(t+\Delta t) & = \boldsymbol{x}_p(t) + (\boldsymbol{U}_p(t) - \boldsymbol{U}_d(t))\,\tau_p\left(1-e^{-\frac{\Delta t}{\tau_p}}\right) + \boldsymbol{U}_f\left(\Delta t - \tau_p\left(1-e^{-\frac{\Delta_p}{\tau_p}}\right)\right) \\ & \quad + B\tau_p\sqrt{\Delta t - 2\tau_p\frac{\left(1-e^{-\frac{\Delta t}{\tau_p}}\right)}{\left(1+e^{-\frac{\Delta t}{\tau_p}}\right)}}\boldsymbol{\xi}_x + B\tau_p^2\frac{\left(1-e^{-\frac{\Delta t}{\tau_p}}\right)^2}{\sqrt{2\tau_p\left(1-e^{-2\frac{\Delta t}{\tau_p}}\right)}}\boldsymbol{\xi}_v \\ \boldsymbol{U}_p(t+\Delta t) & = \boldsymbol{U}_p(t)e^{-\frac{\Delta t}{\tau_p}} + \boldsymbol{U}_f\left(1-e^{-\frac{\Delta t}{\tau_p}}\right) + B\sqrt{\frac{\tau_p}{2}\left(1-e^{-2\frac{\Delta t}{\tau_p}}\right)}\boldsymbol{\xi}_v \end{cases} \tag{11}$$

with $\boldsymbol{\xi}_x$ and $\boldsymbol{\xi}_v$ representing independent random variable vectors sampled in a normal distribution. In equation 11, B is a coefficient relating the diffusional properties of the aerosol particle due to Brownian motion:

$$B^2 = \frac{2k_b\theta}{m_p\tau_p} \tag{12}$$

with θ the temperature, k_b the Boltzmann constant and m_p the mass of the particle. For $Re \ll 1$, τ_p can be defined as follows:

$$\tau_p = \frac{\rho_p d_p^2}{18\mu_f}Cu \tag{13}$$

Above, Cu represents the Stokes-Cunningham slip correction factor, computed following the correlation proposed by Cunningham (1910):

$$Cu = 1 + Kn\left(1.257 + 0.4e^{\frac{-1.1}{Kn}}\right) \tag{14}$$

where Kn represents the Knudsen number:

$$Kn = \frac{\lambda}{d_p}, \tag{15}$$

with λ signifying the mean free path of the molecules in the gas and d_p the diameter of the particle. The Knudsen number makes it possible to determine the gas flow regime around the aerosol particle. A value of $\lambda = 72.4$ nm is chosen in this work, corresponding to air in ambient atmospheric conditions.

In the equations of motion for the discrete phase, the fluid velocity at the particle location, noted U_f, is computed by an interpolation scheme from the computed discretized velocity field. Two interpolation schemes have been tested in the present paper: second order Lagrange polynomial and WENO scheme (Liu et al., 1994). The Lagrange polynomial is used to interpolate the level-set ϕ at the particle's position. The fluid velocity at the particle is interpolated using either of the aforementioned schemes. Their detailed description can be found in Appendix A and their impact is examined in the result section. The primary justification for using the WENO approach is the presence of a jump condition at the interface for the velocity field gradient, which can induce error for the classical method.

https://doi.org/10.5194/ar-2026-1
Preprint. Discussion started: 26 January 2026

AEROSOL Research Discussions

4 Modeling procedure

4.1 Computational domain and grid

The simulation domain is set proportional to the size of the drop, i.e., 6 times d_d in length and $3d_d$ in depth and width (this results in the domain having the $2:1:1$ proportions, see Fig. 3). Outflow boundary conditions are imposed for all faces of the domain except for the bottom, which can be a wall or an injection depending on the manner of initialization.

To keep the mesh cells cubic, we chose the number of points to be used in a 3D case as $256 \times 128 \times 128$, and further $512 \times 256 \times 256$. As different sizes of drops are considered, the dimensionless parameter to be considered for comparing these simulations is $d_g/\Delta x$, which represents the number of mesh points inside the drop diameter, these being 42.7 and 85.3 mesh points for our two meshes.

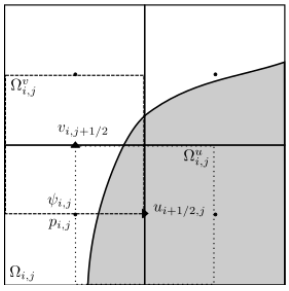

Figure 1. Representation of control volumes Ω on staggered grid.

The initialization condition corresponds to a drop falling in air at rest, starting from its theoretical terminal velocity, as shown in Figure 2. This point avoids expensive numerical simulation if the drop is initialized at rest[1]. In this case, bottom boundary condition is wall (Tanguy, 2004).

An alternate initialization method of the flow was also tested for the highest Reynolds numbers. It corresponds to an initially motionless drop on which air is blown at theoretical terminal velocity from the bottom of the domain. This design aims to reduce the transient time required to eliminate the initial flow perturbations resulting from the nonphysical nature of the original initialization condition, where these perturbations might also be reflected in the drop's oscillations. The impact of using this different initialization condition is shown in the result section below. This alternate initialization is denoted as the blowing configuration, while the original initialization is denoted as the *falling drop* configuration.

4.2 Steady-state criteria

The time advancement of the simulation continues until the drop reaches its terminal fall regime, for which the aerosol capture efficiency is sought. This terminal regime is considered reached when a set of parameters such as the terminal velocity, mean axis ratio, and the oscillation frequency converge towards the literature reference values.

[1]I.e. multiple passes though the domain with a periodic BC until terminal velocity is reached.

https://doi.org/10.5194/ar-2026-1
Preprint. Discussion started: 26 January 2026

AEROSOL Research Discussions

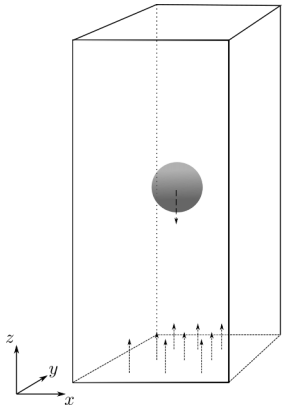

Figure 2. Initialization of the domain using either the configuration of the falling drop (arrow from the drop), with its theoretical terminal velocity present inside of the drop, or initialization of the theoretical terminal velocity at bottom of the domain (arrows from the bottom).

To qualify whether this state is achieved, we introduce the dimensionless time parameter $t^\star$ as the ratio of the physical time t to the integral time scale of the flow past the drop T, i.e. :

$$t^\star = t/T \text{ ; with: } T = \frac{d_d}{\boldsymbol{U}_\infty} \tag{16}$$

$\boldsymbol{U}_\infty$ being the theoretical terminal velocity of the drop (Beard, 1976).

4.2.1 Axis Ratio

The axis ratio (α) is defined as the ratio between the vertical (z-direction) and horizontal (x or y) Feret diameters of the drop, at each time, given by :

$$\alpha(t) = \frac{\max(z|\phi=0) - \min(z|\phi=0)}{\max(x|\phi=0) - \min(x|\phi=0)} \tag{17}$$

where $Max(z|\phi=0)$ corresponds to maximum value of z for which an interface (given by $\phi=0$) is detected.

The value found in the literature corresponds to the mean axis ratio over time.

4.2.2 Oscillation frequencies

The oscillation frequency is defined as the oscillation frequency of the axis ratio (17). It is extracted from the Fast Fourier Transform (FFT) of the axis-ratio time evolution in a steady-state regime.

https://doi.org/10.5194/ar-2026-1
Preprint. Discussion started: 26 January 2026

4.2.3 Oscillation amplitudes

The oscillation amplitudes quantify the maximum extent of the deformations experienced by the drop. Its calculation is presented by the following equation:

$$A_\alpha = \max(\alpha(t)) - \min(\alpha(t)). \tag{18}$$

4.3 Particles initialization

The particles are introduced into the computational domain following the procedure developed by Cherrier et al. (2016) and Dépée et al. (2021) (Figure 3). In this approach, the particles are initialized within a virtual disk (shown in green in Figure 3) located $3d_d$ upstream of the drop center. Their initial radial positions are randomly assigned within this disk of diameter $d_{inj} = d_d + d_p$ to ensure a homogeneous initial distribution. The initial particle velocity is set as the fluid velocity at the position of the injected particle (no slip velocity with respect to the fluid).

The particle diameters in the simulation vary within a range from $2nm$ to $20\mu m$. A density of $1000\ \mathrm{kg.m^{-3}}$ is used so that the geometric and aerodynamic diameters are equal.

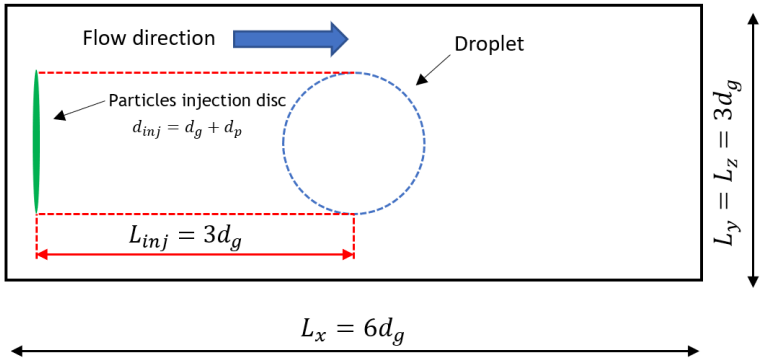

Figure 3. Domain of the simulation.

4.4 Statistical convergence of trajectories

Since Brownian motion is a stochastic process, the convergence of the particle collection efficiency with respect to the number of particles tracked is evaluated by means of the Student's t-test (with a chosen 95% confidence interval) (Biometrika, 1908), after verifying the normality of the data with a Shapiro-Wilk test (Shapiro and Wilk, 1965). This procedure is inspired by Cherrier et al. (2016) and Dépée et al. (2021).

https://doi.org/10.5194/ar-2026-1
Preprint. Discussion started: 26 January 2026

4.5 Particle-flow time coupling

Up to Reynolds numbers of 260 ($Re < 260$), water drops remain perfectly spherical (Beard et al., 1989), and the flow around them is known to be stationary (Pruppacher et al., 1998). These properties are not imposed by the methodology used here, which leaves the interface free, allowing the resolution for the non-stationary flow. Nevertheless, sphericity and stationarity are reproduced by the present model for $Re < 260$ (see Results section and the video supplements tibav:series:1993). In these cases, Lagrangian particle tracking is therefore performed on 'frozen' flows obtained at steady state.

For $Re > 260$, our simulations show oscillations of the drops, associated with unsteady flows when the terminal settling velocity is reached. Thus fully coupled Lagrangian tracking is performed for these cases..

Additionally, a so-called snapshot method is tested as a possible means of reducing the computational time required to derive particle collection efficiencies. This method consists, first, of selecting instantaneous snapshots of the flow field, uniformly distributed in time over several periods of the oscillating steady state regime. Second, particle Lagrangian tracking is performed for each of these frozen velocity fields and the average particle behaviour over all snapshots is derived.This method is expected to give identical results to the time-coupled approach, with a reduced computational effort, if the characteristic flow modulation time is long compared to the particle transit time in the domain.

5 Results for spherical drop regimes

The approach is first verified and validated in the range of Reynolds numbers for which drops are perfectly spherical ($Re < 260$), which is well documented in the literature. Here we adopt the definition of AIAA (1998) for the model verification and validation (V&V): validation is "the process of determining the degree to which a model is an accurate representation of the real world from the perspectives of the intended uses of the model", and verification is "the process of determining that a model implementation accurately represents the developer's conceptual description of the model and the solution to the model".

For drops known from the literature to remain perfectly spherical at terminal velocity ($Re < 260$; Pruppacher et al. (1998); Beard and Chuang (1987)), the following parameters are verified:

- grid independence of velocity field and drop terminal velocity;
- statistical convergence of particles collection efficiencies (see section 4.4), evidenced through confidence intervals;
- independence of particles collection efficiencies with respect to the grid resolution used for the carrier phase, and to fluid velocity interpolation scheme (see 3.2).

Then, the model is validated by comparison with the following reference data:

- drop terminal velocity : measurements by Beard (1976);
- velocity field for the two continuous phases : simulation data of Cherrier et al. (2016);

https://doi.org/10.5194/ar-2026-1
Preprint. Discussion started: 26 January 2026

– particles collection efficiencies : simulation data of Cherrier et al. (2016);

5.1 Verification and validation for the continuous phases

Figure 4 presents a qualitative comparison for a $Re = 30$ simulated drop, as well as the streamlines of the flow. Figure 5 and 6 compares the velocity profiles computed for two grid resolutions and that reported by Cherrier et al. (2016), for $Re = 30$ and 70, on two axes passing by the drop center : along the gravity direction (z-axis) and on the y-axis. Reference profiles of Cherrier et al. (2016) are plotted for comparison. It can be seen that the finest mesh reproduces the behavior of the velocity inside and outside the drop with good agreement. Nevertheless, half a radius away from the drop in the y direction, velocity profiles divert from reference data, whichever the mesh used. This suggests that the boundary conditions may be too close to the drop to accurately capture the flow at that distance. However, this should not affect the trajectories of particles close to the interface.

Additionally, Table 1 reports the computed terminal velocity and the corresponding reference values of Beard (1976). Results show that, regarding the predicted flow field and terminal velocity of the drop, grid-independent results are already obtained for a $128 \times 128 \times 256$ grid, with differences of 0.24% and 3.16% from the terminal velocity for Reynolds drops 30 and 70, respectively. Refinement on a $256 \times 256 \times 512$ grid leads to variations of velocities smaller than 0.90%

d_d (μm)	Re	Mesh	Mesh size ($\Delta x/d_g$)	U_∞ Beard (1976) ($m.s^{-1}$)	U_∞ (present) ($m.s^{-1}$)	relative difference (%)
334	30	$128 \times 128 \times 256$	0.023	1.30	1.30	0.244
		$256 \times 256 \times 512$	0.012		1.30	0.181
503	70	$128 \times 128 \times 256$	0.023	2.03	1.97	3.17
		$256 \times 256 \times 512$	0.012		2.01	0.881

Table 1. Obtained terminal velocities for drops of Reynolds number 30 and 70 for two mesh sizes.

5.2 Verification and validation for the discrete phase

The flow field being verified and validated for the carrier phase, the verification and validation process is being pursued for aerosol particle dynamics. Figures 7 and 8 thus present the collection efficiency obtained for $Re = 30$ and $Re = 70$ respectively, for the two different mesh resolutions employed and for the two fluid velocity interpolation schemes employed. The corresponding reference data of Cherrier et al. (2016) is plotted for validation.

The results show a grid convergence towards the reference results of Cherrier et al. (2016). However, a slight difference persists even with the finest employed mesh, for particle in the Greenfield gap. The Greenfield gap (Greenfield, 1957) refers to the range of particle diameters for which the collection efficiency is minimum (ranging approximately from 50 nm to 3 μm here). We determined that this discrepancy is associated with velocity field interpolation inaccuracies at the particle position

https://doi.org/10.5194/ar-2026-1
Preprint. Discussion started: 26 January 2026

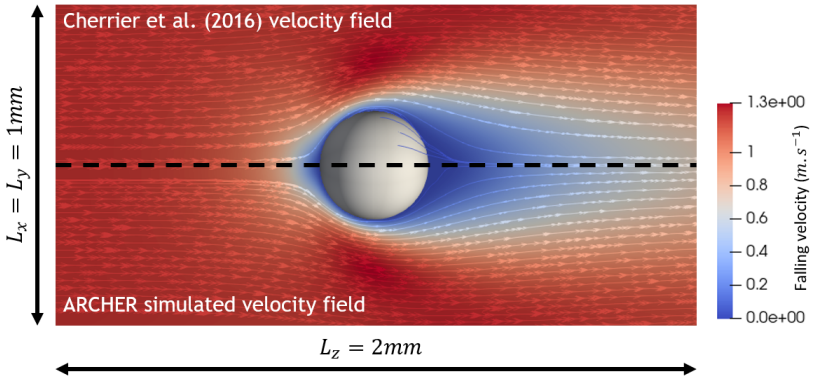

Figure 4. Stationary flow from Cherrier et al. (2016) for a drop of $Re = 30$, compared to the one from the present simulation.

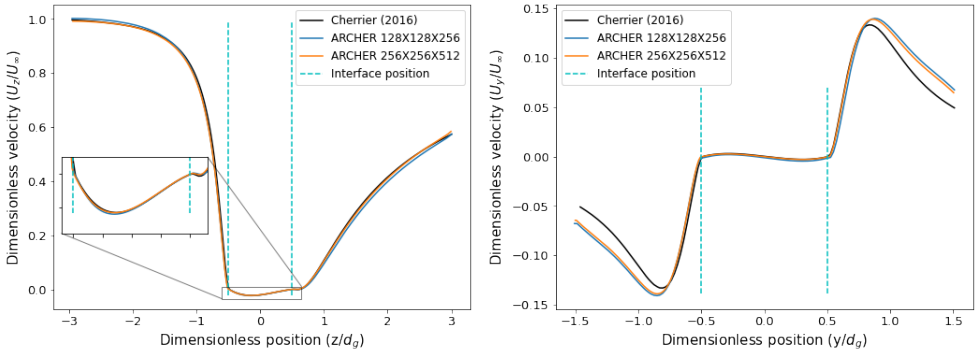

Figure 5. Velocity profiles comparisons for our Re 30 simulations and Cherrier et al. (2016) simulations.

when the particle is close to the interface, where the interpolation schemes, within their stencil, take velocities that are part of the velocities inside the drop. This effect is particularly noticeable for Greenfield gap particles, that show long grazing trajectories since they behave almost like perfect fluid tracers (Belut, 2019). For these trajectories, minor interpolation errors easily lead to erroneous capture of particles by the drop surface.

Overall, results exhibit the highest accuracy for particles with purely Brownian ($d_p \lesssim 50$ nm) or purely inertial ($d_p \gtrsim 3$ μm) behavior. For these size ranges, the predicted collection efficiency differs from the reference by less than 6% and 1% for the polynomial and WENO interpolation schemes, respectively, with the finest mesh employed.

Hence, as regards the collection efficiency, both interpolation methods converge to reference values as the flow mesh size decreases. However, Figure 9 shows that a spatial bias of particle collection patterns on the drop surface exists for the polynomial interpolation scheme and not for the WENO scheme. This is exemplified in this figure by the initial and final positions of particles captured by the drop surface (for $Re = 70$ and $d_p = 2$ μm). Spurious alignment of final particle positions is found for the polynomial scheme, while these final positions should be distributed following a statistically axially symmetric pattern.

https://doi.org/10.5194/ar-2026-1
Preprint. Discussion started: 26 January 2026

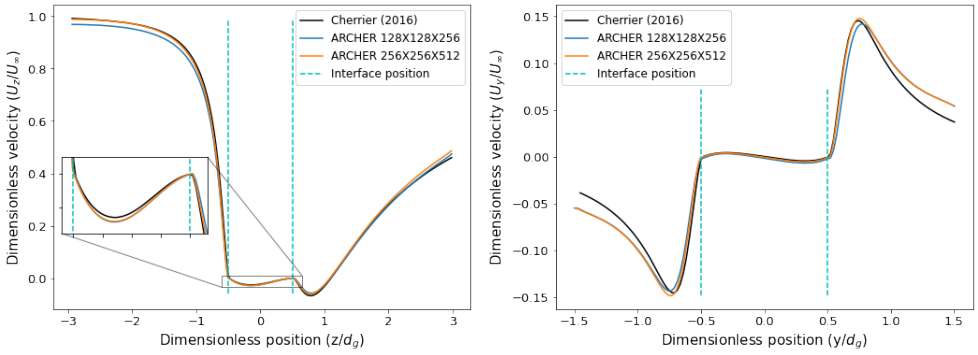

Figure 6. Velocity profiles comparisons for our Re 70 simulations and Cherrier et al. (2016) simulations.

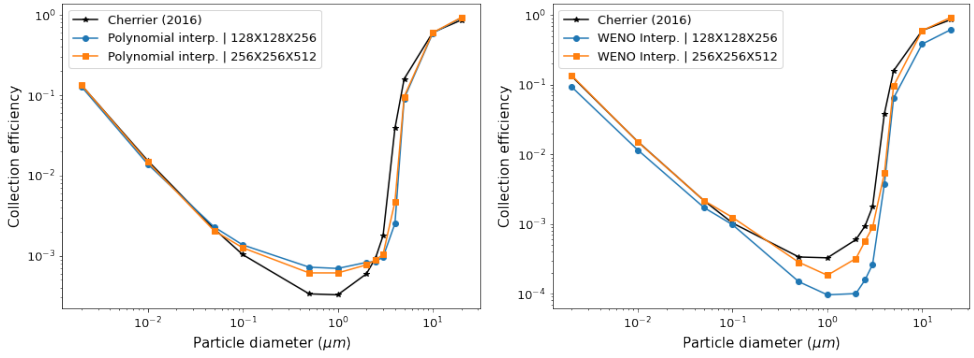

Figure 7. Collection efficiency results for a Re 30 drop using different configurations: Polynomial interpolation (left) and WENO interpolation (right) and comparison with Cherrier et al. (2016) (black curve).

Subsequently, only the WENO scheme is retained to interpolate the fluid velocity at the particles location, since it appears both more precise and less spatially biased than the polynomial scheme. Regarding these results, the finest tested mesh ($256 \times 256 \times 512$) provides the most accurate agreement with Cherrier et al. (2016), and therefore, this will be the mesh used for further simulations. It is worth noting that the mesh is finer than necessary to resolve the dynamics of the continuous phases – but not fine enough to calculate the collection efficiency of aerosol particles in the Greenfield gap with an absolute error lower than about 10^{-3}.

6 Results for non-spherical oscillating drop regimes

We will now consider the case of deforming drops falling at $Re > 500$. Computations are performed for drop diameters of 1.39 mm and 2 mm, corresponding to terminal Reynolds numbers of 500 and 876, respectively (see online supplementary animations tibav:series:1993). In this flow regime, the droplets experience substantial deformations, oscillations, and vortex releases; also much less reference data exist for validation.

https://doi.org/10.5194/ar-2026-1
Preprint. Discussion started: 26 January 2026

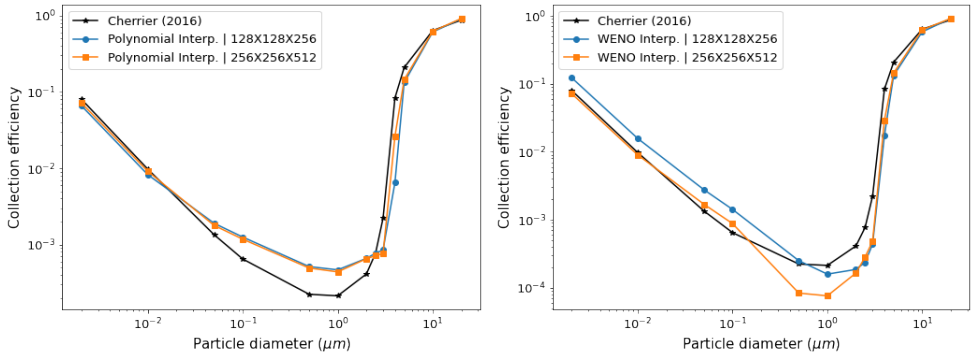

Figure 8. Collection efficiency results for a Re 70 drop using Polynomial interpolation (left) and WENO interpolation (right) and comparison with Cherrier et al. (2016) (black curve).

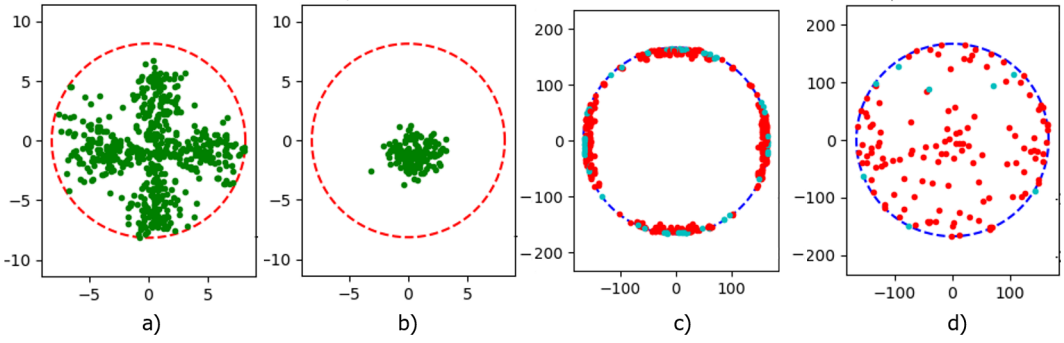

Figure 9. Initial (a,b) and final (c,d) positions of captured aerosol particles for $d_p = 2\ \mu m$ and $Re = 70$ using polynomial (a,c) and WENO (b,d) interpolation respectively (coordinates in μm). For initial position graphs (a,b), the dashed line marks the perimeter of the injection disk; for final position graphs (c,d), the dashed line marks the drop cross section, red dots correspond to particles impacts on the drop front face (stream-wise) and light blue dots correspond to particles impacts on the rear face

6.1 Verification and validation for the continuous phases

For deformable drops, modeling verifications for the motion of the continuous phases are carried out with regard to:

- independence of drop terminal velocity, mean axis-ratio and oscillation frequency from the initialization condition (falling drop vs. blowing configuration);
- statistical stationarity of drop velocity and axis-ratio;

The model is then validated by comparison with the following reference data:

- drop terminal velocity: measurements by Beard (1976);
- drop mean axis ratio and oscillation frequency: data of Szakáll et al. (2010);

https://doi.org/10.5194/ar-2026-1
Preprint. Discussion started: 26 January 2026

AEROSOL Research Discussions

6.1.1 Independence from initialization condition

The influence of flow initialization method (i.e. the falling drop configuration or the blowing configuration) is examined below, in Figure 10, which shows the temporal evolution of the axis ratio and terminal velocity for both configurations, for a 1.39 mm drop ($Re = 500$). Experimental reference data by Beard (1976); Beard et al. (1991) are also shown for comparison.

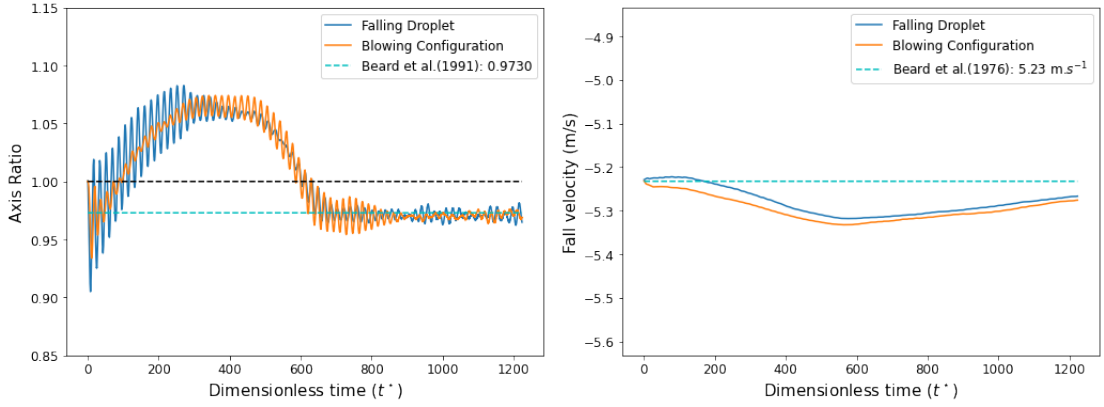

Figure 10. Evolution of axis ratio (left) and the falling velocity of the drop (right) over time for a 1.39 mm drop.

For both configurations, a similar temporal evolution of the axis ratio and terminal velocity is found. In the early stages of the simulation, the drop undergoes oscillations that result in an elongated, prolate shape, characterized by an axis ratio exceeding unity, as the wake of the drop develops. For both initialization methods, there is a period of fast fluctuations visible in Fig. 10 (left). They represent shape perturbations due to the imposed initial velocity in the first init method (blue line), as expected above in the context of Fig. 2. Meanwhile, the second init method (orange line) allows dumping of thise primary perturbations (for $t < 400$). Here, however, once the droplet picks up the momentum from the surrounding airflow ($400 < t < 800$) secondary oscillations appear, only to dissipate once fall velocity is reached. In both cases, this oscillatory behavior is transient and a stationary oscillatory regime with an oblate drop shape is reached while the axis ratio converges towards the values reported in the literature (Beard et al., 1991). During the early transient stage, the drop's fall velocity slightly increases and then tends asymptotically toward the value of the Beard (1976) model, coinciding with the moment when the axis ratio also enters its relaxation stage. No significant influence of the chosen initialization condition is observed on the mean axis ratio, oscillation frequency, and terminal velocity in the pseudo-stationary regime. The physical (and computational) time necessary to reach steady-state is also identical for both initialization strategies. Steady-state is reached after 677 and 448 $t^\star$ for the 1.39mm and 2 mm drop diameters respectively. Further on, we hence retain only the use of the blowing configuration as initialization.

6.1.2 Physical parameters at drop settling velocity

Drop terminal velocity, mean axis-ratio, oscillation amplitude and oscillation frequency are extracted from the pseudo-stationary regime reached by the drop and are presented in Table 2, together with literature reference data, for the two considered drop

https://doi.org/10.5194/ar-2026-1
Preprint. Discussion started: 26 January 2026

Parameter	Configuration	d_d	Szakáll et al. (2010)[1] Beard (1976)[2]	present	relative difference (%)
Axis Ratio	Falling drop	1.39 mm	0.973(1)	0.971	0.174
	Blowing			0.971	0.206
Oscillation amplitude	Falling drop		0.0365(1)	0.0238	35.0
	Blowing			0.0361	1.24
Oscillation frequency	Falling drop		200 Hz(1)	215 Hz	7.51
	Blowing			197 Hz	1.31
Falling velocity	Falling drop		5.23 $m.s^{-1}$(2)	5.27 $m.s^{-1}$	0.70
	Blowing			5.28 $m.s^{-1}$	0.88
Axis Ratio	Falling drop	2 mm	0.93(1)	0.938	0.804
	Blowing			0.935	0.500
Oscillation amplitude	Falling drop		0.0569(1)	0.0592	4.04
	Blowing			0.0466	18.1
Oscillation frequency	Falling drop		122 Hz(1)	127 Hz	4.32
	Blowing			118 Hz	3.13
Falling velocity	Falling drop		6.40 $m.s^{-1}$(2)	6.60 $m.s^{-1}$	3.13
	Blowing			6.59 $m.s^{-1}$	3.01

Table 2. Main dynamic data obtained for the continuous phases and comparison with results from Szakáll et al. (2010) and Beard (1976), for both initialization conditions.

diameters (1.39 and 2 mm). For these four quantities, the deviations from available experimental data are respectively less than 3%, 0.5%, 18% and 3% for the Reynolds tested and simulations' blowing configuration. The coupled flow dynamics in and around the drop appear correctly captured by the model.

6.2 Verification and validation for the discrete phase

Having assessed the quality of the modeling of the continuous phases, we now turn to the evaluation of the modeling of the discrete phase. We examine first the effect of the chosen time coupling method (fully time-coupled Lagrangian tracking vs. snapshot method, see 4.5).

https://doi.org/10.5194/ar-2026-1
Preprint. Discussion started: 26 January 2026

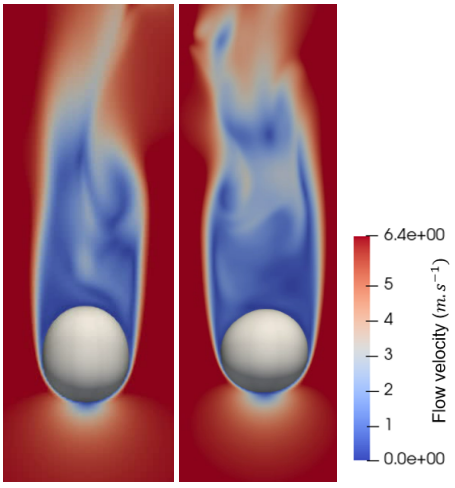

Figure 11. Different flow velocities and morphologies for a 2 mm drop, with a prolate shape (left) (at 250 t*) corresponding to the initial transient phase which later acquires an oblate shape (right) (at 605 t*).

6.2.1 Effect of time coupling method on E

In this section, the necessity of a fully unsteady simulation is evaluated for a 2 mm drop in free fall ($Re = 876$). We first present results obtained with the snapshot method : collection efficiencies E are determined using a series of Lagrangian particle trackings performed on frozen flow fields at different phases of the drop oscillation. Figure 12 (left) shows the efficiencies obtained for the ϕ_i time positions shown in the inset. For readability, statistical uncertainties on E arising from repeated Lagrangian tracking (see 4.4) are not shown here. We observe that for similar phases in the oscillation cycle (similar α and $\dot{\alpha}$), comparable collection efficiencies are calculated (e.g.:$E_{\phi_2} \approx E_{\phi_6}$). In contrast, the collection efficiencies obtained for drop shapes that are similar but in phase opposition during the oscillation cycle (similar α but opposite $\dot{\alpha}$) exhibit significant differences, especially around the minimum of efficiency (e.g.:$E_{\phi_2} \neq E_{\phi_4}$, especially for $d_p \approx 2$ μm). This result suggests that the collection efficiency is influenced not only by the shape of the drop, which logically dictates geometric contact, but also by its deformation dynamics, which induce significant changes in the flow within the gas boundary layer and, consequently, in the collection efficiency.

The mean numerical efficiency $\langle E(d_p)\rangle_\phi$ over the entire oscillation cycle of the drop is then shown in Figure 12 (right). It is calculated as the average of $E(d_p)$ over computed snapshots ϕ_i, i.e. $\langle E(d_p)\rangle_\phi = \sum_{i=1..8} E_{\phi_i}(d_p)$. The uncertainty on $\langle E(d_p)\rangle_\phi$ arising from the limited number of snapshots used and from the number of Lagrangian tracking used for each snapshot is computed by classical error propagation, assuming both effects are uncorrelated. The largest relative statistical uncertainties on $\langle E(d_p)\rangle_\phi$ are found for $dp = 3$ μm.

The collection efficiency obtained with Lagrangian tracking coupled in time with the flow is also shown in Figure 12 (right) for comparison. For this result, Lagrangian tracking is performed during the full simulated stationary oscillating regime, i.e. between $t^\star = 605$ and $t^\star = 1000$.

https://doi.org/10.5194/ar-2026-1
Preprint. Discussion started: 26 January 2026

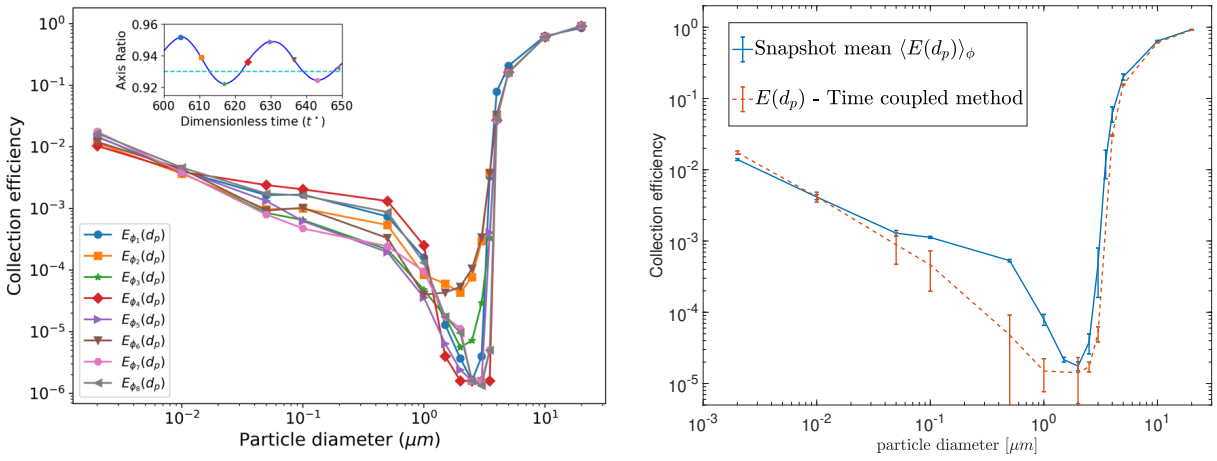

Figure 12. Collection efficiencies calculated for different snapshots of the drop oscillation cycle (left) and the comparison between their corresponding mean $\langle E(d_p)\rangle_\phi$ and time-coupled simulation (right).

It is apparent from Figure 12 (right) that the snapshot method and the time-coupled method provide similar results outside the Greenfield gap, i.e. for inertia-dominated particles ($d_p \gtrsim 3$ μm) and diffusion-dominated particles ($d_p \lesssim 50$ nm), while collection efficiencies predicted by the two methods differ by up to one order of magnitude in the intermediate region, where no particular collection mechanism dominates. This behavior is easily explained by recognizing the tracer behavior of Greenfield gap particles, which are therefore the most sensitive to flow modulations, taken wrongly into account by the snapshot method. This underscores the necessity of performing Lagrangian tracking coupled in time with the flow to accurately capture the collection efficiency in the Greenfield gap.

6.2.2 Comparison with experimental measurement of E

For deforming and oscillating drops falling at terminal velocity, few validation experimental data exist regarding their aerosol collection efficiencies (Lai et al., 1978; Quérel et al., 2014). When these data are available, the knowledge of the true size distribution of employed aerosol particles is of particular matter, since the collection efficiencies vary very sharply with particle size (as visible in Figures 7, 8 and 12). To the best of our knowledge, the measurements from Quérel et al. (2014) are the only ones found in the literature with an accurate aerosol size distribution: we thus employ those for validation. However, Quérel et al. (2014) measured mass collection efficiencies over a whole particle size distribution – not number collection efficiencies resolved with particle sizes. Presently simulated collection efficiencies need hence first to be converted to equivalent collection efficiencies before performing the comparison. The *experimentally equivalent* mass collection efficiency E_m is computed by integrating $E(d_p)$ over the experimental probability density function (PDF) of aerosol particles diameters following :

https://doi.org/10.5194/ar-2026-1
Preprint. Discussion started: 26 January 2026

$$E_m(f) = \frac{\int_0^\infty E(d_p) f(d_p) d_p^3 \mathrm{d}d_p}{\int_0^\infty f(d_p) d_p^3 \mathrm{d}d_p} \tag{19}$$

where $f(dp)$ is the experimentally measured number probability density function of aerosol particles diameters, provided by Quérel et al. (2014). E_m is hence defined for each experimentally tested aerosol probability density function f. These PDF being characterized through their mass mean particle diameter d_m with $d_m = \frac{\int_0^\infty d_p f(d_p) d_p^3 \mathrm{d}d_p}{\int_0^\infty f(d_p) d_p^3 \mathrm{d}d_p}$, we adopt the same abscissa d_m than Quérel et al. (2014) and compare $E_m(d_m)$ obtained either numerically from present work or experimentally by Quérel et al. (2014) in Figure 13.

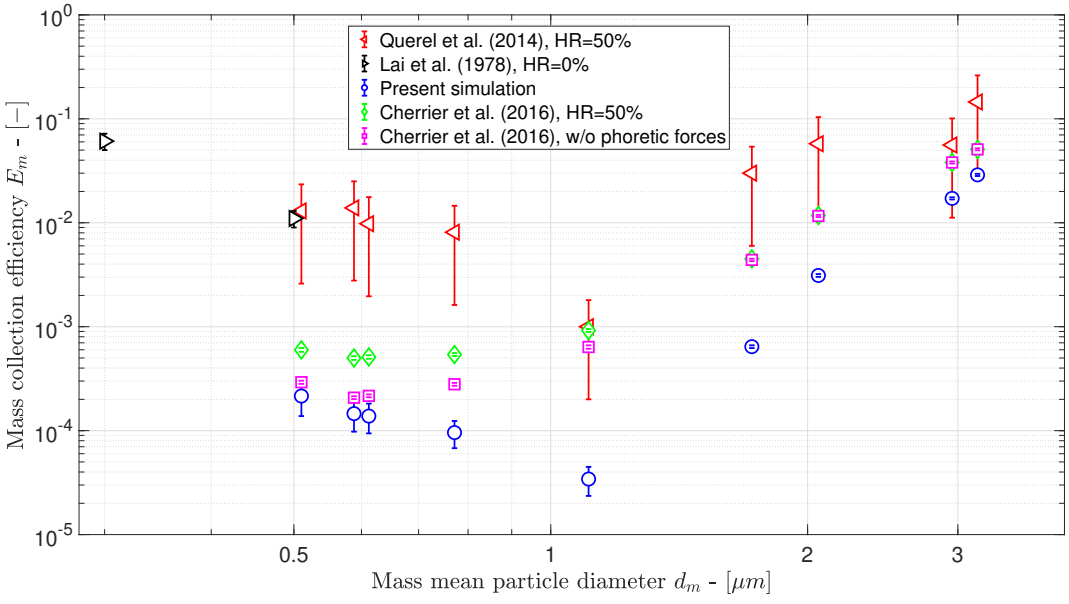

Figure 13. Mass collection efficiencies obtained in the experimental conditions of Quérel et al. (2014) for a $2mm$ drop in free fall ($Re = 876$) : measurements versus simulations and existing correlations

Note that Quérel et al. (2014) experimental results were obtained in sub-saturated air conditions (relative humidity close to 50%), indicating the existence of diffusiophoretic (Ebel et al., 1988) and thermophoretic (Talbot, 1981) forces acting on aerosols due to drop evaporation, while current numerical results do not take these forces into account. For reference, Figure 13 then also displays :

- collection efficiencies measured by Lai et al. (1978), for which the exact aerosol particles PDF is unknown and for which the carrier gas is nitrogen (presumably 0% humidity and active phoretic forces)
- theoretical values obtained by integrating the correlation for E proposed by Cherrier et al. (2016) on experimental PDF f (as in equation 19), in the operating conditions of Quérel et al. (2014) (RH=50%). This correlation extends the

https://doi.org/10.5194/ar-2026-1
Preprint. Discussion started: 26 January 2026

correlation of Wang et al. (1978) with particles inertia effect and thus takes into account phoretic forces, particles inertia and Brownian diffusion;

- theoretical values obtained similarly with the correlation of Cherrier et al. (2016), but without the contribution of phoretic forces.

Note that the correlation of Wang et al. (1978) extended by Cherrier et al. (2016) is used here beyond the drop Reynolds range for which it was established ($Re \lessapprox 200$ with no drop deformation/oscillation). This model therefore provides approximate results, which only allow appreciating the order of magnitude of the impact of phoretic forces, as a possible cause of discrepancy between simulation results and experimental measurements. In Figure 13, uncertainties are derived by classical error propagation from (19), taking into account statistical uncertainties on $E(d_p)$ and experimental uncertainties on $f(d_p)$. Uncertainties on Cherrier et al. (2016) results account solely for experimental uncertainties on $f(d_p)$ provided by Quérel et al. (2014).

Figure 13 shows that measurements from Quérel et al. (2014) and Lai et al. (1978) are similar. However, as Lai et al. (1978) neither provide the size distribution of the aerosol particles nor the relative humidity, it is preferred to compare our model to Quérel et al. (2014). We see that both theoretical and experimental collection efficiencies present the usual "V" shape trend, with a minimum of efficiency for $d_m \approx 1$ μm (Greenfield gap). However, all models underestimate measurements by typically one order of magnitude, and the uncertainties considered are not sufficient to explain the differences. Assuming that the model of Wang et al. (1978), extended by Cherrier et al. (2016), provides a fair approximation of the magnitude of phoretic effects in the conditions of the experiment, it seems that phoretic forces are not sufficient either to explain the discrepancies (the predicted increase of E does not exceed a two-fold increase). However, we cannot rule out the limitations of these models, which are based on the assumption of a spherical symmetry of vapor and temperature fields around the drop, with a first order correction to account for non negligible Reynolds numbers that break this symmetry. This approximation is not calibrated for the present situation that involves drop Reynolds numbers higher than 200: Lemaitre et al. (2020) recently hypothesized, based on a comparison between their experimental results and the Wang et al. (1978) model (and subsequently Cherrier et al. (2016)'s model), that the correlation underestimates phoretic effects for larger drops. To evaluate this hypothesis, the methodology could be extended to determine more exactly the contribution of phoretic forces in this drop size range, by resolving energy and vapor mass fraction conservation equations around the evaporating drop, but this is beyond the scope of present article.

7 Discussion and conclusion

A DNS-VOF-Level Set approach was coupled to Lagrangian discrete particle tracking to model the scavenging of airborne particles by a single free-falling water drop, making it possible to take into account the effect of the complex drop dynamics on particles scavenging in case of oscillating regimes and of drop deformation. Both the effect of drag force and Brownian motion on particles trajectories were accounted for.

This approach enables us to predict the main physical quantities associated with fluid flows inside and outside the drop, as

https://doi.org/10.5194/ar-2026-1
Preprint. Discussion started: 26 January 2026

well as the dynamics of the gas-liquid interface: for the stationary laminar regime (Re=30 and Re=70) – the drop's terminal velocity, the sphericity of its interface and the internal and external velocity profiles – are all correctly predicted. For the unsteady regime with interface deformation and oscillation – the results are validated in terms of drop terminal velocity, mean axis-ratio, axis-ratio oscillation amplitude and frequency. For these 4 quantities, the deviations from available experimental data are respectively less than 3%, 0.5%, 18% and 3% for the Reynolds numbers of 500 and 876 tested and for the blowing configuration of simulations.

For the dispersed aerosol phase, validation by comparison with literature data is less conclusive. In the fall regime where drops remain spherical, the collection efficiency E is both qualitatively and quantitatively accurate, provided that the mesh is sufficiently refined and the interpolation method is robust enough: a maximum deviation for E of 10^{-3} is thus observed in the Greenfield gap, where E is minimum. This is because the effects of Brownian motion and inertia, which are the only effects leading to particle collection, are very small in this range. As a result, any inaccuracy in the velocity calculated at the particle location (due to an insufficiently refined mesh) or any oscillations introduced by the interpolation method contribute significantly and erroneously to E. Here, the use of the WENO scheme provides greater accuracy and limits the nonphysical alignment of particles with the grid. Nevertheless, the fluid mesh used here remains insufficiently fine to achieve an accuracy better than about 10^{-3} on E. It should be noted that Cherrier et al. (2016) had to use a 2.3 times higher spatial resolution in the vicinity of the drop interface to obtain grid-independent results on the collection efficiency, in an axisymmetric 2D space, and that such a resolution is beyond our current computational capabilities in DNS. However, compared to the physical range of variation of E, the inaccuracy of the present model remains small for spherical drops.

In unsteady conditions with deformation and oscillation of the drop, a direct validation of the spectral collection efficiencies $E(d_p)$ is not as straightforward as previously performed for spherical drops, since, to our knowledge, no similar unsteady simulations exist. An indirect validation is proposed, by comparison with Quérel et al. (2014) measurements of E that are integrated over poly-disperse particle size distributions. For this comparison, deviations between simulations and experiments for the collection efficiency typically reach one order of magnitude in the aerosol size range tested, even though the typical (V-shaped) trend of collection efficiency as a function of aerosol size is correctly predicted by the model. Such a difference is significant, but it should first be remembered that it is in line with the variability found in the literature for this parameter, whether obtained experimentally or numerically. The two main reasons are, on the one hand, the steepness of the collection efficiency rise in the inertial regime, which makes E very sensitive to small uncertainties in particle diameters, and, on the other hand, the diminishing of E in the Greenfield gap, which makes the signal-to-noise ratio very small in this particle size range: the result is a high sensitivity to measurement uncertainties or numerical errors.

Beyond these general remarks, it is difficult to attribute the discrepancy between simulation and experiment to one particular cause, as several factors clearly contribute to it. The first is, of course, the numerical uncertainty in particle trajectories already mentioned, linked to the imprecision of air velocity calculated at particle position. Future work will have to focus on improving this accuracy. A second factor of uncertainty arises from the hygrometry and temperature conditions under which the validation data of Quérel et al, were obtained: in these conditions of low relative humidity (RH=50%) and thermal imbalance, the drops

https://doi.org/10.5194/ar-2026-1
Preprint. Discussion started: 26 January 2026

present a non-negligible evaporation rate, with a gradient of vapor fraction and temperature at the liquid-gas interface. These gradient induces diffusionphoresis and thermophoresis on the particles, which are known to increase collection efficiency in the Greenfield gap by typically one order of magnitude (Wang et al. (1978); Cherrier et al. (2016)). These effects are not taken into account in the present simulations, which correspond to the isothermal case without evaporation. In the present case, the bias induced by not taking these phoretic forces into account can be roughly evaluated using correlations for E from the literature, as shown on Figure 13. These correlations suggest that phoretic forces could explain an increase in E by a factor of 2, which is still far from the discrepancy existing between simulation and experiment, which is more in the ratio of 20:1. This evaluation is approximate, however, as the correlation of Cherrier et al. (2016); Wang et al. (1978) are not established for $Re \gtrapprox 200$. Finally, the last factor likely to contribute significantly to the discrepancy between simulations and experiment is metrological, for as already mentioned, E measurement remains a delicate exercise sensitive to numerous difficulties, in particular the control of electrostatic charges on drops and aerosols, which can greatly increase collection efficiency (Wang et al. (1978); Dépée et al. (2021)), and the control of test aerosol particle sizes. Indeed, Quérel et al. (2014)'s measurements are based on the mass of collected particles, and a very small number of particles of larger diameter than those measured could have affected the measurements, since not only are such particles very efficiently collected, but they also contribute to the total mass in proportion to the cube of their diameter. The existence of such particles in the experiment cannot be ruled out, due to aggregation phenomena (linked to the high aerosol concentrations required to obtain a measurable efficiency), and due to the inherently partial control of aerosol size distribution in the experiment (sampling-based control). It should also be noted that the aerosol particles used were hygroscopic and that an increase in their diameter during the experiment, due to heterogeneous nucleation of water vapor, cannot be ruled out. In addition, the flow upstream of the drops in the experiments may not have been at rest as in the simulations. Upstream turbulence could potentially affect the collection efficiency. All these possible experimental biases make it difficult to isolate the role of any particular mechanism.

The paper also evaluated the interest of deriving E from Lagrangian trackings performed on flow snapshots over the drop oscillation cycle. This method was found suitable for particles outside the Greenfield gap (presently for $d_p \lesssim 50$ nm or $d_p \gtrsim 3$ μm). However, for the particles in the Greenfield gap, this method is not justified, since it predicts E values that are too far away from those calculated by Lagrangian trackings coupled in time with the flow. Flow/particle time coupling is then highly recommended to obtain reliable results. We may add that the snapshot method is based on the assumption that the flow seen by the particles is quasi-stationary. This is justifiable if the characteristic times of drop oscillation and flow modulation are large compared with the transit time of the particles around the drop. In practice, drop oscillation periods are respectively 19 and 27 $t^\star$ for Reynolds numbers of 500 and 876: hence, these periods are actually comparable to the mean particle transit times around the drop (which range typically between 10 and 20 $t^\star$ for the particle diameters considered, as shown in Belut (2019)). This explains why the snapshot method is not reliable here.

In conclusion, this article reports on a first attempt to simulate the collection of aerosols by a deformable water drop falling transiently through still air. While the flow dynamics of the continuous phases appear to be correctly predicted, the results

https://doi.org/10.5194/ar-2026-1
Preprint. Discussion started: 26 January 2026

highlight a number of points for improvement in the prediction of the dynamics of the dispersed phase: the accuracy of interpolation of air velocity at the particle position in the drop boundary layer, the need for coupled dynamic calculation for all 3 phases, and the interest - for certain ambient conditions - of taking into account heat exchange and water phase changes to account for the contributions of phoretic forces and Stefan flow on capture. The collection of aerosol particles by deformable free-falling drops is therefore still a matter of research.

Data availability. Numerical data will be made available upon reasonable request to the authors.

Video supplement. Supplementary animations showing the interaction between the flow past the deforming drop and aerosol particles of various aerodynamic diameters are provided (tibav:series:1993).

Author contributions. Conceptualization: T. Ménard, P. Lemaitre and E. Belut; Funding acquisition: T. Ménard, P. Lemaitre and E. Belut; Formal analysis: T. Ménard, E. Reyes and E. Belut; Investigation: E. Reyes; Methodology: T. Ménard, W. ki and E. Belut; Project administration: T. Ménard, P. Lemaitre and E. Belut; Resources: T. Ménard ; Software : T. Ménard, E. Reyes, W. ki; Supervision: T. Ménard, P. Lemaitre and E. Belut; Validation: T. Ménard, P. Lemaitre and E. Belut; Visualization: E. Reyes, T. Ménard and E. Belut; Writing (original draft preparation): E. Reyes, T. Ménard, E. Belut and P. Lemaitre; Writing (review and editing): all co-authors.

Competing interests. The authors declare no competing interests

Acknowledgements. The present work was performed using computing resources of CRIANN (Normandy, France). Financial support was obtained with the grant RIN COLLAGE provided by the region of Normandy, IRSN (Institut de Radioprotection et de Sûreté Nucléaire) and INRS (Institut national de recherche et de sécurité).

Appendix A: Appendix A

- Lagrange Polynomial interpolation

To interpolate any scalar Φ (i.e. level set, velocity component) in 3D, on a point (x, y, z), with a N-degree polynomial $P(x, y, z)$, we have the following formula :

https://doi.org/10.5194/ar-2026-1
Preprint. Discussion started: 26 January 2026

$$
\begin{aligned}
P(x,y,z) &= \sum_{k=0}^{N}\sum_{j=0}^{N}\sum_{i=0}^{N}\Phi_{i,j,k}L_i^{(x)}(x)L_j^{(y)}(y)L_k^{(z)}(z) \quad \text{; with:}\\
L_i^{(x)}(x) &= \prod_{l=0,l\neq i}^{N}\frac{x-x_l}{x_i-x_l}\\
L_j^{(y)}(y) &= \prod_{m=0,m\neq j}^{N}\frac{y-y_m}{y_j-y_m}\\
L_k^{(z)}(z) &= \prod_{n=0,n\neq k}^{N}\frac{z-z_n}{z_k-z_n}
\end{aligned}
\tag{A1}
$$

In the case of $N = 2$, used here for level set and velocities, the 27 points stencil is centered on the particle and no specific treatment is done for velocity near the interface. That means gas and liquid velocities can be used together to approximate these on the particle and assess any errors on interpolation evaluation due to discontinuities of velocity gradients.

- WENO Interpolation

The Weighted Essentially Non-Oscillatory (WENO) schemes represent a class of high-order accurate schemes specifically engineered for solving problems characterized by piecewise smooth solutions that may contain discontinuities. The fundamental concept behind these schemes revolves around the precision of the approximation process. Instead of employing a fixed stencil for interpolation, WENO schemes utilize a nonlinear adaptive approach.

This adaptive procedure dynamically selects the locally smoothest stencils, effectively minimizing the risk of crossing or interpolating through discontinuities within the domain. Without this selection, the interpolation process might inadvertently incorporate, in the same stencil, velocity information from both sides of the interface, potentially leading to erroneous interpolated values, especially where velocity gradient jumps occur at the interface, as in the present case.

Then, because we are in finite volume framework, any velocity component $\bar{u}$ of $\boldsymbol{U}$ given by the Navier-Stokes solver is a cell averaged function. The 5^{th} WENO (or ENO) approaches initially developed by (Shu, 1997) permits to interpolate velocity at the center of particle or to compute an average velocity inside a volume containing the particle. Both are developped and converge when $r_p << \Delta x$, but only the second method is detailed here.

A two-dimensional schematic of this procedure is found in Figure A1. The desired average velocity (noted U_f and standing for any component of the velocity) is inside the dashed square ($S_p = [x_p - r_p, x_p + r_p] \times [y_p - r_p, y_p + r_p]$) surrounding the particle p whose center of mass is located in the control volume $\Omega_{i,j}^{\bar{u}} = [x_{i-1/2}, x_{i+1/2}] \times [y_{j-1/2}, y_{j+1/2}]$ of the corresponding velocity component $\bar{u}$.

The mean velocities $U_{f,j-2}...U_{f,j+2}$ are first computed with the help of interpolation in x-direction and then the average velocity U_f on S_p is determined by interpolation of these values on the y-direction.

The computation of $U_{f,j}$ follows:

$$
U_{f,j} = \sum_{r=0}^{k-1}\omega_r(x_p)U_{f,j}^{(r)}(x_p), \tag{A2}
$$

https://doi.org/10.5194/ar-2026-1
Preprint. Discussion started: 26 January 2026

AEROSOL Research Discussions

where $k = 3$ for WENO 5^{th}. In (A2), $U_{f,j}^{(r)}(x_p)$ is computed with the help of velocity values inside the stencil I_r :

$$U_{f,j}^{(r)}(x_p) = \Big(F_j^{(r)}(x_p + r_p) - F_j^{(r)}(x_p - r_p)\Big)\frac{\Delta x}{2 \times r_p}$$

and the following approximation of a primitive of velocity (Shu (1997)):

$$\begin{aligned} F_j^{(r)}(x) - K &= \sum_{s=0}^{k-1} \bar{u}_{i-r+s,j} \sum_{m=s+1}^{k} \prod_{\substack{l=0 \\ l\neq m}}^{k} \frac{x - x_{i-r+l-\frac{1}{2}}}{x_{i-r+m-\frac{1}{2}} - x_{i-r+l-\frac{1}{2}}} \\ &= \sum_{s=0}^{k-1} c_{rs}(x)\bar{u}_{i-r+s,j}. \end{aligned} \tag{A3}$$

The weighted coefficients $\omega_r(x_p)$ in (A2) are defined by :

$$\omega_r(x_p) = \frac{\alpha_r(x_p)}{\sum_{k=0}^{k-1} \alpha_k(x_p)} \tag{A4}$$

with the "MwenoZ" method (Hu et al. (2016)) to compute $\alpha_r(x_p)$ (also β_r, ϵ and ζ) coefficients :

$$\alpha_r(x_p) = d_r(x_p)\Big(1 + \frac{\zeta}{\beta_r + \epsilon}\Big). \tag{A5}$$

Generally $d_r(x_p)$ coefficients are computed in such a way, allowing the recovery of the 5^{th} order in smoothed region. Because particles are mobile – i.e the coefficients d_r have to be recalculated at each time step – the stability condition $\omega_r > 0\ \forall r$ is, in general, not respected (Shu (1997); Shi et al. (2002)). This might imply the appearance of no-physical particle trajectories. Thus, we have decided to weight each stencil using a sinusoidal function (A6) whose argument is relative to the particle position x_p, as presented at the bottom of the Figure A1, ensuring it takes only positive values. A consequence of this, however, is the loss of 5^{th} order in smoothed region.

$$\begin{aligned} d_0 &= \frac{\pi}{4\Delta x} \int_{x_{i+1/2}}^{x_p+\Delta x} \cos\Big(\frac{\pi}{2\Delta x}(x - x_p)\Big)dx \\ d_1 &= \frac{\pi}{4\Delta x} \int_{x_{i-1/2}}^{x_{i+1/2}} \cos\Big(\frac{\pi}{2\Delta x}(x - x_p)\Big)dx \\ d_2 &= \frac{\pi}{4\Delta x} \int_{x_p-\Delta x}^{x_{i-1/2}} \cos\Big(\frac{\pi}{2\Delta x}(x - x_p)\Big)dx. \end{aligned} \tag{A6}$$

Finally, the same procedure is applied in the y-direction, where the velocity on the particle is :

https://doi.org/10.5194/ar-2026-1
Preprint. Discussion started: 26 January 2026

AEROSOL Research Discussions

$$U_f = \sum_{r=0}^{k-1} \omega_r(y_p) U_f^{(r)}(y_p)$$

with

$$U_f^{(r)} = \left(G^{(r)}(y_p + r_p) - G^{(r)}(y_p - r_p) \right) \frac{\Delta y}{2 \times r_p}$$

and

$$\begin{aligned} G^{(r)}(y) - K &= \sum_{s=0}^{k-1} U_{f,j-r+s} \sum_{m=s+1}^{k} \prod_{\substack{l=0 \\ l \neq m}}^{k} \frac{y - y_{j-r+l-\frac{1}{2}}}{y_{j-r+m-\frac{1}{2}} - y_{j-r+l-\frac{1}{2}}} \\ &= \sum_{s=0}^{k-1} c_{rs}(y) U_{f,j-r+s}. \end{aligned} \tag{A7}$$

The global method therefore uses a 125 points stencil in three dimensions, and because velocity components have different locations, this procedure differs for each of them.

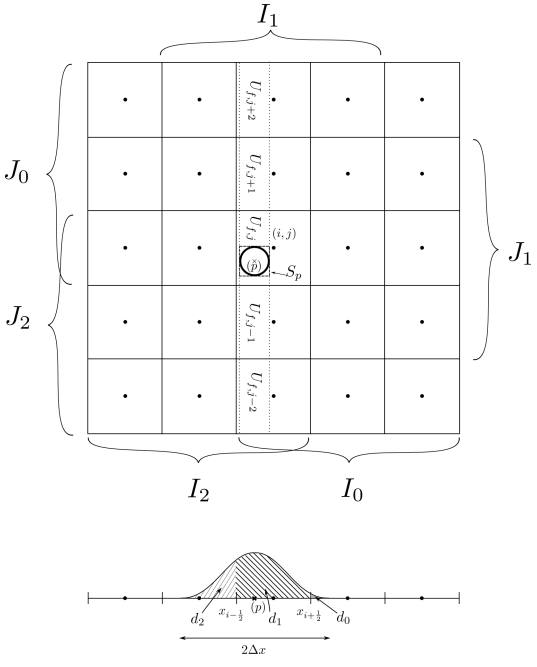

Figure A1. Illustration of 2D, 25 point stencil used to interpolate the mean velocity on square surrounding the particle. I_r and J_r represented sub-stencil in x-direction and y-direction respectively. The coefficient d_r used to weight velocity computed by each stencil (I_r here) is symbolize by the area under a sinusoidal curve of period equals $2\Delta x$ and centered on the particle position.

https://doi.org/10.5194/ar-2026-1
Preprint. Discussion started: 26 January 2026

References

AIAA: Guide for the Verification and Validation of Computational Fluid Dynamics Simulations (AIAA G-077-1998 (2002)), American Institute of Aeronautics and Astronautics, Inc., 1998.

Aniszewski, W., Ménard, T., and Marek, M.: Volume of Fluid (VOF) type advection methods in two-phase flow: A comparative study, Computers & Fluids, 97, 52 – 73, https://doi.org/http://dx.doi.org/10.1016/j.compfluid.2014.03.027, 2014.

Beard, K.: Terminal Velocity and Shape of Cloud and Precipitation Drops Aloft, Journal of the Atmospheric Sciences, 33, 851–864, 1976.

Beard, K. V. and Chuang, C.: A new model for the equilibrium shape of raindrops, Journal of the Atmospheric sciences, 44, 1509–1524, 1987.

Beard, K. V., Ochs III, H. T., and Kubesh, R. J.: Natural oscillations of small raindrops, Nature, 342, 408–410, 1989.

Beard, K. V., Kubesh, R. J., and Ochs, H. T.: Laboratory measurements of small raindrop distortion. Part I: Axis ratios and fall behavior, Journal of the atmospheric sciences, 48, 698–710, 1991.

Belut, E.: Collecte des aérosols par les gouttes : impact du phénomène de capture arrière en régime laminaire stationnaire, in: Proceedings of CFA 2019 - Congrès Français sur les Aérosols 2019, Paris, France, https://doi.org/10.25576/ASFERA-CFA2019-16616, 2019.

Biometrika, S.: The probable error of a mean, Biometrika, 6, 1–25, 1908.

Cherrier, G., Belut, E., Gerardin, F., Tanière, A., and Rimbert, N.: Aerosol particles scavenging by a droplet: Microphysical modeling in the Greenfield gap., Atmos. Environ., 166, 519–530, 2016.

Cunningham, E.: On the Velocity of Steady Fall of Spherical Particles through Fluid Medium, The Royal Society Publishing, 83, 357–365, 1910.

Dépée, A., Lemaitre, P., Gelain, T., Monier, M., and Flossmann, A.: Laboratory study of the collection efficiency of submicron aerosol particles by cloud droplets-Part I: Influence of relative humidity., Atmospheric Chemistry and Physics, 21, 6945–6962, 2021.

Duret, B., Reveillon, J., Menard, T., and Demoulin, F.: Improving primary atomization modeling through {DNS} of two-phase flows, International Journal of Multiphase Flow, 55, 130 – 137, https://doi.org/http://dx.doi.org/10.1016/j.ijmultiphaseflow.2013.05.004, 2013.

Ebel, J., Anderson, J. L., and Prieve, D.: Diffusiophoresis of latex particles in electrolyte gradients, Langmuir, 4, 396–406, 1988.

Elgobashi, S.: Prediction of the particle-laden jet with a two-equation turbulence model., Journal of Multiphase Flow, 10, 687–710, 1984.

Greenfield, S. M.: Rain scavenging of radioactive particulate matter from the atmosphere, Journal of Meteoroly, 14, 115–125, 1957.

Grover, S. N. and Pruppacher, H. R.: A Numerical Determination of the Efficiency with Which Spherical Aerosol Particles Collide with Spherical Water Drops Due to Inertial Impaction and Phoretic and Electrical Forces., Journal of the Atmospheric Sciences., 34, 1655–1663, 1977.

Hu, F., Wang, R., and Chen, X.: A modified fifth-order WENOZ method for hyperbolic conservation laws, Journal of Computational and Applied Mathematics, 303, 56–68, https://doi.org/https://doi.org/10.1016/j.cam.2016.02.027, 2016.

Lai, K.-Y., Dayan, N., and Kerker, M.: Scavenging of aerosol particles by a falling water drop, Journal of Atmospheric Sciences, 35, 674–682, 1978.

Lemaitre, P., Sow, M., Quérel, A., Dépée, A., Monier, M., Menard, T., and Flossmann, A.: Contribution of phoretic and electrostatic effects to the collection efficiency of submicron aerosol particles by raindrops, Atmosphere, 11, 1028, 2020.

Liu, X.-D., Osher, S., and Chan, T.: Weighted essentially non-oscillatory schemes, Journal of computational physics, 115, 200–212, 1994.

Ménard, T., Tanguy, S., and Berlemont, A.: Coupling level set/VOF/ghost fluid methods: Validation and application to 3D simulation of the primary break-up of a liquid jet, International Journal of Multiphase Flow, 33, 510–524, 2007.

https://doi.org/10.5194/ar-2026-1
Preprint. Discussion started: 26 January 2026

Min, C. and Gibou, F.: A second order accurate level set method on non-graded adaptive cartesian grids, Journal of Computational Physics, 225, 300–321, https://doi.org/https://doi.org/10.1016/j.jcp.2006.11.034, 2007.

Minier, J. P. and Peirano, E.: The pdf approach to turbulent polydispersed two-phase flows., Physics Reports, 352, 1–3, 1–214, 2001.

Mohaupt, M., Minier, J. P., and Tanière, A.: A new approach for the detection of particle interactions for large-inertia and colloidal particles in a turbulent flow., International Journal of Multiphase Flow, 37, 746–755, 2011.

Popinet, S.: Numerical Models of Surface Tension, Annual Review of Fluid Mechanics, 50, 49–75, https://doi.org/10.1146/annurev-fluid-122316-045034, 2018.

Pruppacher, H. R., Klett, J. D., and Wang, P. K.: Microphysics of clouds and precipitation, 1998.

Quérel, A., Lemaire, P., Monier, M., Porcheron, E., Flossmann, A. I., and Hervo, M.: An experiment to measure raindrop collection efficiencies: influence of rear capture, Atmospheric Measurement Techniques, 7, 1321–1330, 2014.

Ren, W., Reutzsch, J., and Weigand, B.: Direct Numerical Simulation of Water Droplets in Turbulent Flow, Fluids, 5, https://doi.org/10.3390/fluids5030158, 2020.

Shapiro, S. S. and Wilk, M. B.: An analysis of variance test for normality (complete samples), Biometrika, 52, 591–611, 1965.

Shi, J., Hu, C., and Shu, C.-W.: A Technique of Treating Negative Weights in WENO Schemes, Journal of Computational Physics, 175, 108–127, https://doi.org/https://doi.org/10.1006/jcph.2001.6892, 2002.

Shu, C.-W.: Essentialy Non-Oscillatory and Weighted Essentially Non-Oscillatory Schemes for Hyperbolic Conservation Laws, NASA Langley Research Center, 1997.

Slinn, W. G. N.: Some Approximations for The Wet and Dry Removal of Particles and Gases from the Atmosphere., International Journal of Multiphase Flow, 1977.

Sussman, M. and Puckett, E. G.: A Coupled Level Set and Volume-of-Fluid Method for Computing 3D and Axisymmetric Incompressible Two-Phase Flows, Journal of Computational Physics, 162, 301–337, https://doi.org/https://doi.org/10.1006/jcph.2000.6537, 2000.

Sussman, M., Smereka, P., and Osher, S.: A Level Set Approach for Computing Solutions to Incompressible Two-Phase Flow, Journal of Computational Physics, 114, 146–159, https://doi.org/https://doi.org/10.1006/jcph.1994.1155, 1994.

Szakáll, M., Mitra, S., Karolina, D., and Stephan, B.: Shapes and oscillations of falling raindrops - A review, Journal of the Atmospheric Sciences, 97, 416–425, 2010.

Talbot, L.: Thermophoresis-a review, Progress in Astronautics and Aeronautics, 74, 467–488, 1981.

Tanguy, S.: Développement d'une méthode de suivi d'interface. Applications aux écoulements diphasiques, Ph.D. thesis, Université de Rouen, 2004.

Tanguy, S. and Berlemont, A.: Application of a level set method for simulation of droplet collisions, International journal of multiphase flow, 31, 1015–1035, 2005.

tibav:series:1993: Collection of aerosol particles by falling deformable drops, CORIA, https://doi.org/10.5446/s_1993, https://doi.org/10.5446/s_1993.

Vaudor, G., Ménard, T., Aniszewski, W., Doring, M., and Berlemont, A.: A consistent mass and momentum flux computation method for two phase flows. Application to atomization process., Computers and Fluids, 152, 204–216, 2017.

Wang, A., Song, Q., and Yao, Q.: Behavior of hydrophobic micron particles impacting on droplet surface, Atmospheric Environment, 115, 1–8, 2015.

Wang, P. K., Grover, S. N., and Pruppacher, H. R.: On the Effect of Electric Charges on the Scavenging of Aerosol Particles by Clouds and Small Raindrops., Journal of the Atmospheric Sciences, 35, 1735–1743, 1978.

https://doi.org/10.5194/ar-2026-1
Preprint. Discussion started: 26 January 2026

620 Welch, J. E., Harlow, F. H., Shannon, J. P., and Daly, B. J.: The MAC method-a computing technique for solving viscous, incompressible, transient fluid-flow problems involving free surfaces, Tech. rep., Los Alamos National Lab.(LANL), Los Alamos, NM (United States), 1965.